Simultaneous small- and wide-angle scattering at high X-ray energies

J. E. Daniels,[a,b] D. Pontoni,[a]* Rui Ping Hoo[b] and V. Honkimäki[a]*

[a]ID15, European Synchrotron Radiation Facility, Grenoble, France, and [b]School of Materials Science and Engineering, University of New South Wales, Sydney, Australia.
E-mail: diego.pontoni@esrf.fr, honkimak@esrf.fr

Combined small- and wide-angle X-ray scattering (SAXS/WAXS) is a powerful technique for the study of materials at length scales ranging from atomic/molecular sizes (a few angstroms) to the mesoscopic regime ($\sim$1 nm to $\sim$1 μm). A set-up to apply this technique at high X-ray energies ($E > 50$ keV) has been developed. Hard X-rays permit the execution of at least three classes of investigations that are significantly more difficult to perform at standard X-ray energies (8–20 keV): (i) *in situ* strain analysis revealing anisotropic strain behaviour both at the atomic (WAXS) as well as at the mesoscopic (SAXS) length scales, (ii) acquisition of WAXS patterns to very large q (>20 Å^{-1}) thus allowing atomic pair distribution function analysis (SAXS/PDF) of micro- and nano-structured materials, and (iii) utilization of complex sample environments involving thick X-ray windows and/or samples that can be penetrated only by high-energy X-rays. Using the reported set-up a time resolution of approximately two seconds was demonstrated. It is planned to further improve this time resolution in the near future.

1. Introduction

Advanced functional and structural materials often exhibit multiple-length-scale structures which greatly enhance their properties. Characterization techniques which do not reveal the existence of such hierarchical structural organizations often fail to properly account for the macroscopic properties of these advanced materials. The ability to probe *simultaneously* the structure over multiple length scales is therefore increasingly becoming a necessary requirement for materials scientists, condensed matter physicists and chemists who aim at understanding the microscopic origin of the macroscopic properties of both natural and man-made smart functional/structural materials.

The combination of small-angle X-ray scattering (SAXS) and wide-angle X-ray scattering (WAXS) has proven to be particularly successful for the characterization of materials simultaneously at the atomic and mesoscopic length scales (Gurun *et al.*, 2009; Hennessy *et al.*, 2004; Baldrian *et al.*, 2002; Pontoni, Bolze *et al.*, 2003; Bolze *et al.*, 2004). Applied at high X-ray energies (50–100 keV), these combined techniques offer new experimental possibilities (Haeffner *et al.*, 2005). Here, we show that at high X-ray energies three important factors differentiate the technique from its lower-energy counterpart. Firstly, the scattering/diffraction angles decrease at a rate inversely proportional to the energy, therefore the

WAXS signal is compressed in the forward direction and the X-ray momentum transfer vectors lie very near to the plane perpendicular to the incident X-ray beam. This is crucial for *in situ* experiments where perturbations such as stresses (Steuwer *et al.*, 2009) or electric fields (Daniels, 2008) are applied uni-axially to the sample. This allows for example the possibility to analyze independently and simultaneously the diffraction from sets of grains having orientations parallel or perpendicular to the perturbing field. This information is critical in the understanding of anisotropic effects in polycrystalline materials. In addition, it also allows rapid quantification of sample texture (Ischia *et al.*, 2005).

Secondly, owing to the compression of WAXS information in the forward direction, collection of scattering signals up to high momentum transfer [$q = 4\pi\sin(\theta)/\lambda$, where 2θ is the scattering angle and λ is the X-ray wavelength] is possible on a single flat-panel detector (Chupas *et al.*, 2003). In addition, extraction of the atomic pair distribution functions (PDFs) from WAXS data yields important information about the local structure of materials (Egami & Billinge, 2003). This is a particularly useful data analysis technique when observing the structural behaviour of amorphous and nano-crystalline materials. The simultaneous acquisition of SAXS data yields complementary information about particle size, shape and polydispersity, thus favouring a comprehensive understanding of the nano-particulate systems under study. In addition,

SAXS is sensitive also to peculiar core-shell or more complex mesoscopic morphologies, which can arise for example in the frequent cases when hard nanoparticles are coated with soft organic molecular layers in order to reduce, control or prevent their coagulation or sintering. On the other hand the amorphous *versus* crystalline character of the nanoparticle core material is directly evident from the overall features of the WAXS profiles. In the case of single-crystal nanoparticles, the WAXS patterns exhibit the conventional sharp powder diffraction rings related to the atomic-scale long-range order present in the nanoparticle cores. The nanoscopic size of the crystallites induces a broadening of the powder diffraction peaks thus allowing estimation of the particle size by means of the Scherrer formula and related peak-shape analysis methods (Vorobiev *et al.*, 2008). The results of the latter methods can be compared with the size values obtained from the analysis of the SAXS patterns. However, most nanomaterials are polycrystalline, semicrystalline or completely amorphous, with the additional complication that the nanoparticles are often moderately to considerably polydisperse. In such situations, the standard Scherrer and peak-shape analyses give only limited and uncertain results. In this context, applying the PDF method can become particularly useful. If the WAXS data collection is extended out to sufficiently large q values, the PDF method becomes sensitive to the short-range atomic/molecular order/disorder present in the nanoparticle cores. In particular, the evolution of this short-range order/disorder can be monitored *in situ* for example across thermal treatment of various nanomaterials. On the other hand, if the WAXS pattern is extended also towards the low-q regime, the obtained PDF $g(r)$ levels out to the value of 1 at a length-scale comparable with the particle size. This information can again be cross-correlated with the particle size information obtained from the simultaneously collected SAXS data.

The third advantage of using hard X-rays is that the X-ray absorption is dramatically reduced. This makes possible the investigation of thick highly absorbing samples and/or the use of complex sample environments involving thick sample containers such as in the case of high-pressure investigations. In addition, the high penetration power, in combination with small scattering angles, allows the use of small X-ray exit windows in sample environments without sacrificing the access to high q scattering values.

Here, we present initial results from a set-up in which the above three factors can be taken advantage of. The results show the power of such a technique and its importance for the characterization of current and future multi-length-scale materials.

2. Experimental set-up

Experiments were performed at beamline ID15A of the European Synchrotron Radiation Facility (ESRF). A schematic of the experimental set-up is shown in Fig. 1. A beam energy of 69.5 keV with a bandwidth of 300 eV was selected using a double bent Laue silicon crystal (111) monochromator. The beam was then passed through a set of compound refractive lenses that focused the beam at the SAXS detector plane. Slits prior to the monochromator were used to define the beam size and a second set of slits, in vacuum, were positioned just prior to the sample and used as guard slits in order to minimize background scattering. For experiments under load the sample was placed in a Bose electro-force mechanical testing rig, and for static measurements a 2 mm-diameter thin-walled ($\sim$10 µm) borosilicate glass capillary was used. In both cases the sample-to-SAXS-detector distance was 7.70 m, while the WAXS detector distance was varied between 0.3 and 1.5 m depending upon sample type and data
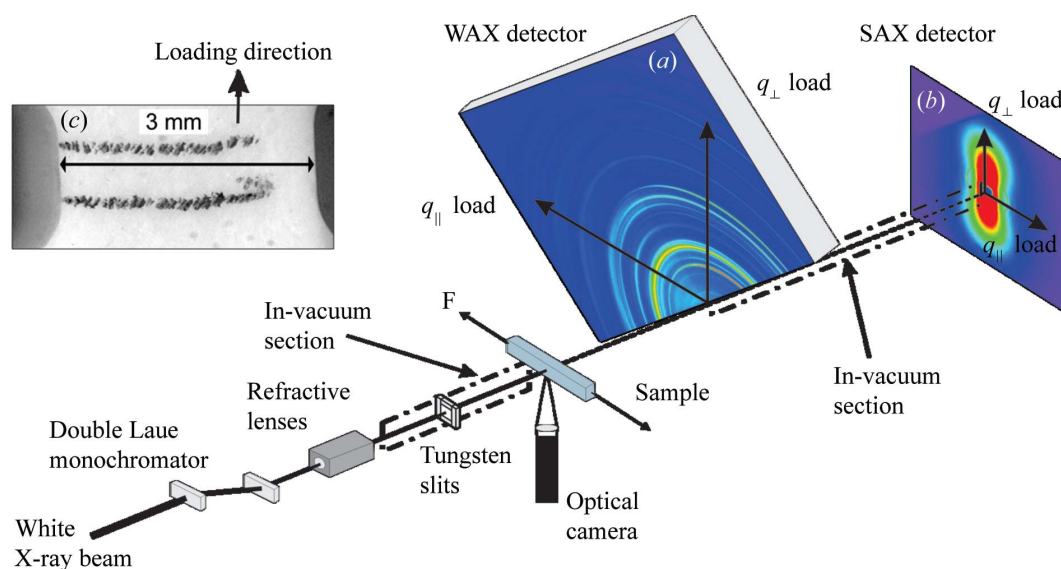
Figure 1
Schematic of the experimental set-up showing principal components. (*a*), (*b*) and (*c*) show examples of the WAXS, SAXS and optical images, respectively. The optical image shown in (*c*) is of a bovine cortical bone tensile specimen used in the multi-length-scale strain analysis described in the main text. The optical image shows the sample surface whose normal is perpendicular to both the load and X-ray beam.

q-range required. The WAXS detector was a Pixium 4700 flat panel (Daniels & Drakapoulos, 2009). This detector is particularly well suited because the border region that is not sensitive to X-rays is relatively small ($\sim$ 30 mm), thus reducing to a minimum the loss of WAXS data in the low-*q* range. For the SAXS signal detection, a Frelon camera equipped with a CsI scintillator and taper optic system was used (Coan *et al.*, 2006). A 5 m vacuum pipe was placed between the WAXS and SAXS detectors in order to remove the air scattering background from the SAXS patterns. It is acknowledged that alternative detector arrangements are possible for collection of the WAXS information, including multiple detectors at various positions around the central beam placed to record a large *q*-range. The set-up described here, however, allows for the collection of a wide (and easily variable) *q*-range at all angles to the applied uni-axial field using a single detector. This reduces complexity and allows for accurate observation of anisotropic material behaviour.

The beamstop to prevent the main beam from impinging the SAXS detector was placed on the inside window of the vacuum pipe. With this configuration the SAXS pattern was obtained over a *q*-range of 0.008–0.23 Å^{-1}. The *q*-range obtained in the WAXS signal varied depending upon the sample to detector distance. While the WAXS detector can be operated at very short distances in order to collect data up to high *q* values ($\sim$ 35 Å^{-1}), this limits the low *q* range obtained owing to the inactive border region of the detector. Fig. 2 shows the *q*-ranges of a CeO$_2$ pattern at two typical working distances of 0.42 and 1.42 m. It should also be noted that obtaining a larger *q*-range on the WAXS detector is possible by further increasing the X-ray energy. In addition, a small adjustment to the set-up allows one to cover a continuous *q*-range from the SAXS to WAXS detector. This is achieved by translating the WAXS area detector sideways so as to intercept the direct beam (which is blocked by an additional cylindrical lead beamstop positioned just before the WAXS detector). This geometry modification prevents the set-up from performing as a truly simultaneous SAXS/WAXS instrument; however, SAXS and WAXS patterns can still be acquired almost simultaneously with a time delay of approximately 15 s between each other.

For the deformation studies, an optical camera was used to record series of real-time images of the sample surface during loading. An example image is shown in Fig. 1(*c*). A digital image correlation method was used to quantify strains by comparing the images captured before and after deformation. The method involves tracking with sub-pixel resolution the displacement of fiducial markers that appear within regions of interest of the optical images (Fig. 1*c*), and hence determining the macroscopic strains parallel and perpendicular to the loading directions (Benecke *et al.*, 2009). This approach is advantageous to such an experimental set-up, as it is a non-contact non-destructive optical method yielding accurate strain values with good time resolution.

3. Results and discussion

3.1. Multi-length-scale strain analysis

An *in situ* deformation study of bovine cortical bone was performed. Bone is a complex multi-length-scale nano-composite material in which a crystalline hydroxyapatite phase is interconnected with a collagen fibre matrix. The concurrent use of high-energy X-ray SAXS and WAXS reveals the texture and strains in the collagen fibrils and in the mineral lattice simultaneously upon *in situ* loading.

The mineral crystals have a plate-like shape, and a hexagonal crystallographic structure (Rho *et al.*, 1998). The *c*-axis of the minerals is highly aligned with the longitudinal direction of the bone, *i.e.* with the bone axis, resulting in strong (002) Bragg peaks along the loading direction. The intensity of the (002) peak diminishes at orientations away from this preferred direction, as shown in Fig. 3. The staggered mineralized collagen fibrils have a periodic spacing of $d \simeq 67$ nm. These fibrils are highly aligned with the mineral crystals along the bone axis, giving rise to a series of Bragg's reflections. The first-order collagen reflection is at $q = 2\pi/d \simeq 0.0094$ Å^{-1} while the third-order collagen peak at $q \simeq 0.028$ Å^{-1} is shown to be very intense (Fig. 3*b*) (Gupta *et al.*, 2006).

Upon tensile loading, both the mineral phase and collagen fibrils are strained. The magnitude of the strain in each phase is calculated by fitting the change in peak position of the (002) Bragg peak in the WAXS pattern and the third-order collagen peak in the SAXS pattern. Results of this analysis as well as the macroscopic strains obtained from the optical image correlation analysis are shown in Fig. 4. These results indicate that at a stress of approximately 62 MPa the sample just began to fail at a local level as suggested by the discontinuity in the collagen strain (blue) and crystallographic strain (green). However, the sampled remained rigid at a macroscopic level because it could still accumulate load and continue to strain
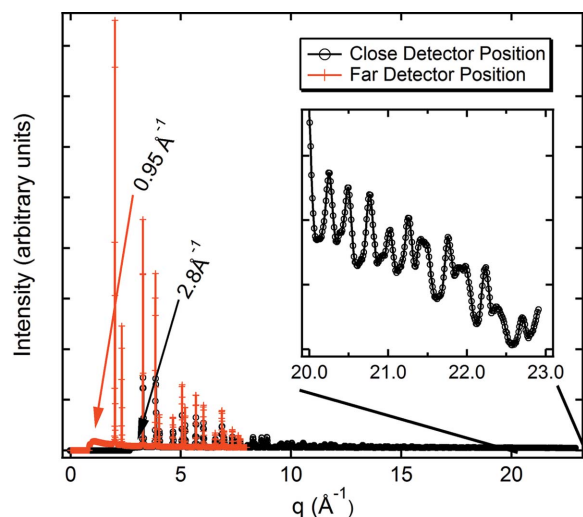
Figure 2
Observed *q*-ranges for the WAXS data of a CeO$_2$ standard powder for detector distances of 420 mm (close) and 1420 mm (far). The increase of the sample-to-detector distance reduces the lowest *q* value accessible in the WAXS image from 2.8 Å^{-1} (close position, black symbols) to 0.95 Å^{-1} (far position, red symbols).
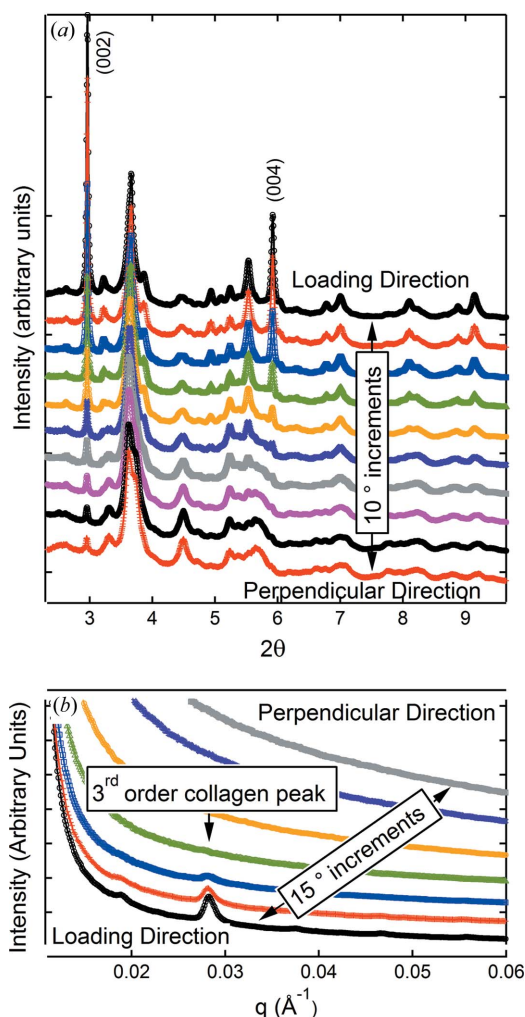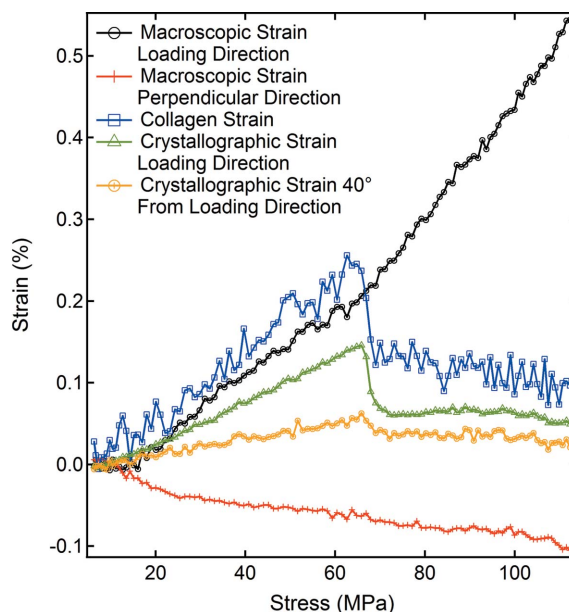
Figure 3
Integration of WAXS (*a*) and SAXS (*b*) images as a function of angle between the loading direction and scattering vector.

with increasing stress (macroscopic strain curve, black symbols in Fig. 4).

3.2. Combined SAXS/PDF studies

As an example for combined SAXS/PDF studies we used water dispersions of magnetite (Fe_3O_4) nanoparticles of 5–6 nm in diameter and at a concentration of ~5% by volume. The particles were rendered hydrophilic by coating them with a double layer of sodium oleate ($C_{18}H_{33}NaO_2$), which also stabilizes them against irreversible aggregation (Vorobiev *et al.*, 2004).
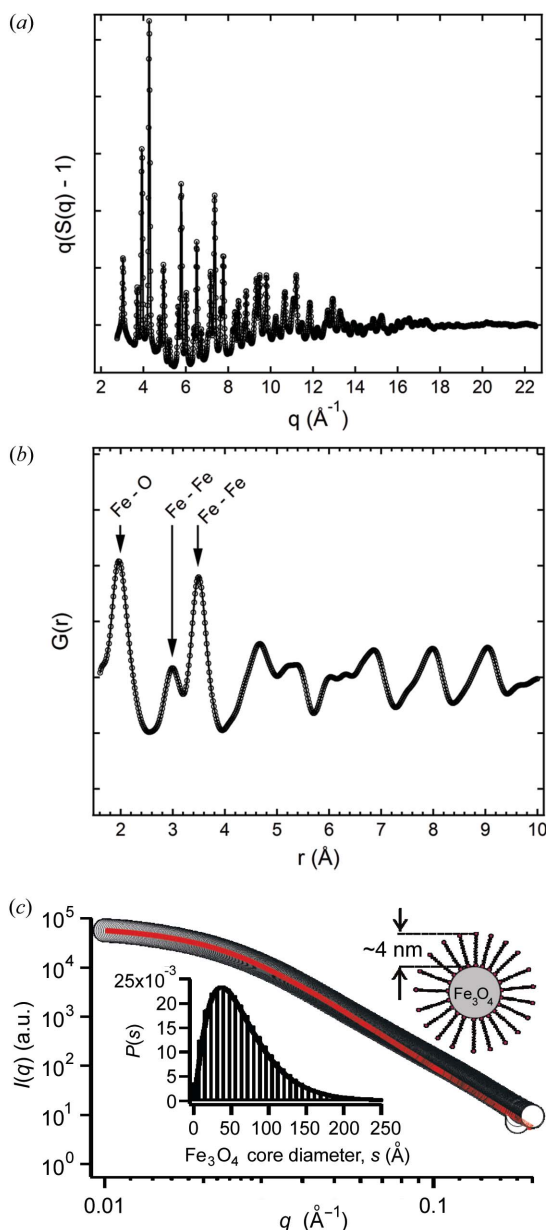
The SAXS profile obtained at 69.5 keV from a 2 mm-thick sample capillary is presented in Fig. 5(*c*). The monotonic character of this profile indicates that the nanoparticle suspension is dilute enough to minimize interparticle interference effects that would lead to the appearance of a local peak related to the structure factor of interparticle local correlations. At the same time the absence of a local minimum suggests that the size distribution of the magnetite nanoparticles is considerably broad. The red line in Fig. 5(*c*) is a fit

Figure 4
Strain information observed in bovine cortical bone during loading. Macroscopic strain was calculated using an image correlation technique from optical images of the sample surface. Fibril strain was calculated using the third-order collagen peak from the SAXS image and lattice strain was calculated from the (002) hydroxiapatite WAXS peak.

to the form factor of a model approximating the particles as core-shell spheres with Schultz size distribution (Pontoni, Finet *et al.*, 2003). The electron densities of the solvent, shell and core are fixed to the bulk values for water (0.334 e $Å^{-3}$), sodium oleate (0.339 e $Å^{-3}$) and magnetite (1.399 e $Å^{-3}$), respectively. The shell thickness is fixed to the double of the length of a fully stretched sodium oleate molecule (2×24 Å). The three fitted parameters are an arbitrary intensity scale factor, the average core size (5.6 ± 0.4 nm) and the size variance (4.2 ± 0.2 nm) of the Schultz core size distribution. The fitted size distribution is shown in the inset of Fig. 5(*c*). It compares well with the one obtained for the same nanoparticles from atomic force microscopy data (Vorobiev *et al.*, 2004).

The WAXS data measured from the same capillary simultaneously with the SAXS pattern are represented as a $q[S(q) - 1]$ versus q profile in Fig. 5(*a*), where $S(q)$ is the scattered intensity normalized to the average atomic form factor of the sample. The first four peaks visible in the low q region of Fig. 5(*a*) correspond to the (400), (422), (511) and (440) Bragg reflections of the bulk magnetite cubic crystal structure. The four lowest-order magnetite Bragg reflections (111), (220), (311) and (222) are not accessible in this configuration but can be measured by translating the WAXS detector position, as outlined in §2. Access to the lowest-order diffraction rings would allow a complete Scherrer/peak-shape analysis; however, this is not meant to be the main strength of the high-energy X-ray set-up presented here. Precise peak-shape analysis of WAXS data would profit from high-resolution powder diffraction instruments at standard X-ray energies, such as the ID31 beamline of the ESRF (Hodeau *et al.*, 1998). The main strength of the current high-energy set-up is

(a)

(b)

(c)

Figure 5
(*a*) WAXS scattered intensity of magnetite Fe_3O_4 nanoparticles in water, represented as $q[S(q) - 1]$, (*b*) atomic PDF calculated from (*a*), and (*c*) SAXS data and fit (red line) to a polydisperse core–shell sphere model with fitted Schultz core size distribution (inset).

Access to the high-*q* regime allows application of the PDF data analysis technique (Egami & Billinge, 2003). The PDF obtained from the profile of Fig. 5(*a*) is shown in Fig. 5(*b*). The missing lowest-order diffraction peaks in the WAXS profile affect only the large-*r* region of the PDF [not shown in Fig. 5(*b*)] where indirect information about the average particle size may be obtained from the *r* range where $G(r)$ stabilizes at the value of 1 (Egami & Billinge, 2003; Peterson *et al.*, 2003). The simultaneous SAXS data prove, however, to be much more powerful for particle size analysis, in particular in cases of highly polydisperse samples such as the one under study here [see Fig. 5(*c*) and inset]. On the other hand the $G(r)$ shown in Fig. 5(*b*) clearly exhibits the first three peaks that are known to be related to the local Fe—O and Fe—Fe atomic distances (Fernandez-Martinez *et al.*, 2010). These data therefore demonstrate that it is possible to monitor simultaneously and with relatively high time-resolution (~1 s) the local atomic structure and the long-range order of the crystalline cores, together with the particle size, shape and polydispersity of magnetite nanoparticles dispersed in water at relatively low concentrations (of the order of 1% volume fraction). These results motivate and open the way to time-resolved investigations of thermally induced size/shape/polydispersity and crystal phase transformations in colloidal magnetite dispersions as an example, and more generally in a broad range of other technologically important engineered smart nano-materials.

The hard-X-ray SAXS/WAXS instrument is currently an optional non-permanent feature of the ID15 beamline that can be reassembled in case of demand. This is planned to become one of the permanent set-ups offered by the future high-energy beamline (UPBL2) that is being designed in the context of the ESRF upgrade program. Such a beamline will also include permanent facilities for X-ray imaging and tomography combined with time-resolved diffraction capabilities. This will further build on the multi-length-scale materials analysis technique demonstrated here and will allow studies of both bulk samples and complex buried interfaces developed by an increasingly interdisciplinary community of materials scientists, physicists, chemists, engineers and life scientists.

the easy access to high-*q* diffraction data using relatively short exposure times. The WAXS profile from a dilute colloidal suspension shown in Fig. 5(*a*) was obtained with an exposure time of just a few seconds for both the WAXS and SAXS detectors. More strongly scattering samples such as those discussed in §3.1 gave statistically relevant profiles with exposure times of just a few hundreds of milliseconds. Many micro- or nano-structured solid samples of interest for materials science are so strongly scattering that they can yield statistically relevant data with exposures of 100 ms or shorter thus allowing highly time-resolved simultaneous high-energy SAXS/WAXS experiments.

4. Conclusions

An experimental set-up for the simultaneous collection of SAXS and WAXS scattering/diffraction data at high X-ray energies has been presented. Studies of the multi-length-scale deformation of a biological nano-composite material (bovine cortical bone) and combined SAXS/PDF analysis of magnetite nanoparticles exemplify the performances of the set-up. We believe that the use of combined high-energy SAXS/WAXS techniques will be critical to complement the already existing and well performing standard-energy X-ray methods for the characterization of multi-length-scale phenomena in many future material classes.

research papers

References

Baldrian, J., Steinhart, M., Vlcek, P., Horky, M., Laggner, P., Amenitsch, H. & Bernstorff, S. (2002). *J. Macromol. Sci. B*, **41**, 1023–1032.

Benecke, G., Kerschnitzki, M., Fratzl, P. & Gupta, H. S. (2009). *J. Mater. Res.* **24**, 421–429.

Bolze, J., Pontoni, D., Ballauff, M., Narayanan, T. & Colfen, H. (2004). *J. Colloid Interface Sci.* **277**, 84–94.

Chupas, P. J., Qiu, X., Hanson, J. C., Lee, P. L., Grey, C. P. & Billinge, S. J. L. (2003). *J. Appl. Cryst.* **36**, 1342–1347.

Coan, P., Peterzol, A., Fiedler, S., Ponchut, C., Labiche, J. C. & Bravin, A. (2006). *J. Synchrotron Rad.* **13**, 260–270.

Daniels, J. E. (2008). *J. Appl. Cryst.* **41**, 1109–1114.

Daniels, J. E. & Drakapoulos, M. (2009). *J. Synchrotron Rad.* **16**, 463–468.

Egami, T. & Billinge, S. J. L. (2003). *Underneath the Bragg Peaks, Structural Analysis of Complex Materials.* Oxford: Elsevier.

Fernandez-Martinez, A., Timon, V., Roman-Ross, G., Cuello, G. J., Daniels, J. E. & Ayora, C. (2010). *Am. Mineral.* In the press.

Gupta, H. S., Seto, J., Wagermaier, W., Zaslansky, P., Boesecke, P. & Fratzl, P. (2006). *Proc. Natl. Acad. Sci. USA*, **103**, 17741–17746.

Gurun, B., Thio, Y. S. & Bucknall, D. G. (2009). *Rev. Sci. Instrum.* **80**, 123906.

Haeffner, D. R., Almer, J. D. & Lienert, U. (2005). *Mater. Sci. Eng. A*, **399**, 120–127.

Hennessy, A., Neville, A. & Roberts, K. J. (2004). *Cryst. Growth Des.* **4**, 1069–1078.

Hodeau, J. L., Bordet, P., Anne, M., Prat, A., Fitch, A. N., Dooryhee, E., Vaughan, G. & Freund, A. (1998). *Proc. SPIE*, **3448**, 353–361.

Ischia, G., Wenk, H.-R., Lutterotti, L. & Berberich, F. (2005). *J. Appl. Cryst.* **38**, 377–380.

Peterson, P. F., Božin, E. S., Proffen, Th. & Billinge, S. J. L. (2003). *J. Appl. Cryst.* **36**, 53–64.

Pontoni, D., Bolze, J., Dingenouts, N., Narayanan, T. & Ballauff, M. (2003). *J. Phys. Chem. B*, **107**, 5123–5125.

Pontoni, D., Finet, S., Narayanan, T. & Rennie, A. R. (2003). *J. Chem. Phys.* **119**, 6157–6165.

Rho, J. Y., Kuhn-Spearing, L. & Zioupos, P. (1998). *Med. Eng. Phys.* **20**, 92–102.

Steuwer, A., Daniels, J. E. & Peel, M. J. (2009). *Scr. Mater.* **61**, 431–433.

Vorobiev, A., Chernyshov, D., Gordeev, G. & Orlova, D. (2008). *J. Appl. Cryst.* **41**, 831–835.

Vorobiev, A., Major, J., Dosch, H., Gordeev, G. & Orlova, D. (2004). *Phys. Rev. Lett.* **93**, 267203.